Segmentation of Female Pelvic Organs in Axial Magnetic Resonance Images using Coupled Geometric Deformable Models

Zhen Ma[a], Renato M. Natal Jorge[b], Teresa Mascarenhas[c], João Manuel R. S. Tavares[d]

[a] *Faculdade de Engenharia, Universidade do Porto, Rua Dr. Roberto Frias, s/n 4200-465 Porto, Portugal*

[b] *IDMEC-Polo FEUP, Departamento de Engenharia Mecânica, Faculdade de Engenharia, Universidade do Porto, Rua Dr. Roberto Frias, 4200-465 Porto, Portugal*

[c] *Hospital de São João, Faculdade de Medicina, Universidade do Porto, Al. Prof. Hernâni Monteiro 4200-319 Porto, Portugal*

[d] *Instituto de Engenharia Mecânica e Gestão Industrial, Departamento de Engenharia Mecânica, Faculdade de Engenharia, Universidade do Porto, Rua Dr. Roberto Frias, 4200-465 Porto, Portugal*

Corresponding Author:

Prof. João Manuel R. S. Tavares

Faculdade de Engenharia da Universidade do Porto (FEUP)

Departamento de Engenharia Mecânica (DEMec)

Rua Dr. Roberto Frias, s/n, 4200-465 PORTO - PORTUGAL

Tel: +315 22 5081487, Fax: +315 22 5081445

Email: tavares@fe.up.pt, Url: www.fe.up.pt/~tavares

Abstract

The segmentation of pelvic structures in magnetic resonance (MR) images of the female pelvic cavity is a challenging task. This paper proposes the use of three novel geometric deformable models to segment the bladder, vagina and rectum in axial MR images. The different imaging appearances and prior shape knowledge are combined into a level set framework as segmentation cues. The movements of the contours are coupled with each other based on interactive information, and the organ boundaries can be segmented simultaneously. With the region-based external forces defined, the proposed algorithms are robust against noise and partial volume effect.

Keywords *Image segmentation; Level set; Prior shape knowledge; Imaging appearance; Bladder; Vagina; Rectum.*

1. Introduction

Pelvic organ prolapse and pelvic floor dysfunction are common clinical conditions affecting a large number of women [1-5]. For example, from 30 to 50% of women in Europe and the USA suffer from urinary incontinence (UI) [4]; by the age of 80, 11.1% of women have undergone operations for pelvic organ prolapse or UI, and many of them have experienced more than one operation [5]. However, the pathophysiology and its relationship with the symptoms are still unclear. Findings from epidemiologic studies are usually inconsistent, because they are not designed to investigate cause-and-effect relationships.

For a patient-specific study, the development of novel and less invasive therapies requires a thorough knowledge of the relationship between the pathophysiology of incontinence and anatomy; an anatomic analysis lays the necessary foundation for understanding the specific mechanical etiologies of pelvic floor disorders [6, 7]. Static magnetic resonance imaging (MRI), especially T2-weighted imaging, is currently a preferred modality for this study [8-10]. The imaging data from MRI have improved the accuracy of clinical diagnoses considerably and assisted the planning of therapeutic strategies. Nevertheless, in order to carry out quantitative analyses or biomechanical simulations, the relevant structures need to be segmented in 2D image slices. This process is presently done by manual segmentation, which is very time consuming (often 1-2 hours) [11, 12] and can lead to results that suffer from intra/inter observer errors, particularly when the images were influenced by noise and partial volume effect [13, 14]. Therefore, effective segmentation algorithms are required.

Due to the complex anatomy, the segmentation of the structures in the pelvic cavity needs to be carried out carefully. Applying the current segmentation algorithms to the female pelvic cavity was discussed in [13], and it was concluded that an effective algorithm should be based on imaging features of the relevant pelvic structure. A deformable model was then proposed in [14], which combined the appearances of pelvic structures with a priori knowledge to handle the segmentation of the levator ani muscles in T2-weighted MR images. A coupled surface evolution algorithm was proposed in [15] to segment the prostate and the bladder in CT images. This approach combines a shape constraint to assist the segmentation and uses a coupling technique to avoid overlapping of the two organs.

However, few algorithms have been proposed to segment the pelvic organs in MR images and most of them are not suitable for T2-weighted MR images [16-18]. For example, the seeded region growing algorithm [19] was proposed to segment the bladder and the rectum in [16] but this algorithm is sensitive to image noise and the initial conditions adopted. A coupled level set framework, which can handle successfully the segmentation of inner and outer bladder walls in T1-weighted MR images, was proposed in [17]. Nevertheless, in T2-weighted images the bladder has different imaging appearances, and the influence of noise and partial volume effect (PVE) is more appreciable.

This paper focuses on the segmentation of axial T2-weighted MR images as the physiological anatomy of the pelvic structures can be clearly identified on these images [7]. Geometric deformable models are among the segmentation techniques that have been intensively studied in recent years. Due to their ability to incorporate various segmentation cues, they are ideal for the segmentation of pelvic structures [13]. In this

paper, a coupling approach is proposed to segment the urinary bladder, vagina and rectum from axial T2-weighted MR images of the female pelvic cavity. The approach uses three novel geometric deformable models that couple with each other, and is able to segment the three organs simultaneously. The distinct imaging appearances of the organs and the prior shape knowledge are incorporated into a level set framework. Using the adopted external forces, the pelvic organs can be segmented accurately even when the images are influenced by noise and PVE. Experiments have given promising results and demonstrated the effectiveness of the proposed approach.

The paper is organized as follows: In Section 2, the female pelvic anatomy and geometric deformable models are reviewed. Section 3 introduces the novel coupling approach along with detailed explanations about the associated equations of motion. Then, in Sections 4 and 5, experiments are presented and discussed. Finally, in the last section, the main contributions are outlined and future works are suggested.

2. Background

2.1 Anatomy and imaging appearance

In axial T2-weighted MR images, the spatial relationship of the pelvic organs can be well depicted; the imaging appearances of the three pelvic organs and surrounding tissues are satisfactorily distinct. An example can be seen in Fig. 1.

[insert Fig. 1 about here]

In the female pelvic cavity, the urinary bladder is a temporary reservoir for urine whose status is closely related to its contents and the state of neighboring organs [22]. The bladder lumen has high signal intensity in T2-weighted MR images due to the urine within it, while the muscular bladder wall has intermediate signal intensity that is similar in appearance to the vaginal and rectal walls.

The vagina is located in front of the rectum and behind the bladder. The widest part of this organ is at the proximal vagina, and then its width decreases as it passes through the pelvic floor [23]. The different layers of the vagina can be observed in T2-weighted axial MR images. The outer muscular layers have homogeneous low signal intensity, while the mucosal layer and the secretions within the vaginal canal have high signal intensity. The appearance of the mucosal layer varies with hormonal stimulation: in women that are before menarche or after menopause, the high signal intensity central strip is very thin; but in women of reproductive age, the high signal intensity central stripe can be seen clearly, especially during the secretory phase [24]. The tissues around the vagina also have high signal intensity that is appreciably lower than the intensity of the bladder lumen but still more similar to the bladder lumen than to the vagina and rectum.

The rectum also has different layers with different appearances. The muscular layer of the rectum has intermediate signal intensity that is distinguishable from the bladder wall; while the rectal lumen, which is bounded by the mucosa and submucosa, has low signal intensity similar to the muscular vaginal wall. The tissues around the rectum have appearances alike those around the vagina.

Given the complex imaging background of the female pelvic cavity, segmentation cannot be carried out merely based on the intensity gradient. Fig. 2 illustrates the segmentation results using the geodesic active contours [25], from which one can see that the gradient information is not a reliable cue for segmentation; the moving contours either stopped incorrectly at places with a high intensity gradient or leaked outside due to the blur caused by noise and PVE.

[insert Fig. 2 about here]

On T2-weighted MR images, compared to the high signal intensity of the bladder lumen, the bladder wall has a low signal intensity appearance that is similar to the muscular layer of the rectum. The fat tissues that surround the vagina and rectum have comparably high signal intensity appearances that are more like the bladder lumen than the two organs. The different appearances of the pelvic structures and the similarity between the layers of organs are valuable cues for segmentation. Moreover, although the imaging appearances of the vagina and rectum are frequently blurred on T2-weighted MR images, their shapes do not change much in an image series under the axial planes; therefore, prior shape information can be used to provide shape guidance. Based on these features, geometric deformable models are used in this paper to segment the three pelvic organs.

2.2 Geometric deformable models

Segmentation by geometric deformable models is carried out through curve evolution. In such a model, the initial contours will follow a speed function and move to the

boundaries of the objects to be segmented. The equation of motion of a geometric deformable model is a level set equation [26]:

$$\phi_t + F\left|\nabla\phi\right| = 0, \tag{1}$$

where $\phi(X,t)$ is the level set function which is normally defined as the signed distance function to the initial contours, and $F(X,t)$ is the speed function.

Due to the implementation of the level set method, the geometric deformable models have low computational complexity and can handle the topological changes during the evolution. The speed function should be defined so that the moving contours are attracted to the desired boundaries; in this process, segmentation cues, restrictions on the movement, and other techniques can be incorporated to the model easily. These features are attractive for medical imaging [13, 27-29]. Based on the anatomy and imaging features of the pelvic cavity, geometric deformable models are suitable to carry out the segmentation.

2.2.1 Multiphase segmentation

If there are more than two regions or structures to be segmented, appropriate strategies should be added to the geometric deformable models. One possibility is to use different level set functions for distinct regions. An effective model was proposed in [30]; the segmentation process was modeled as the minimization of the following energy functional:

$$E\left(\Gamma,\{\alpha_i\}\right) = \sum_{i=1}^{N}\left(\frac{\mu}{2}\int_{\partial R_i} ds - \log\left(P\left(\left\{I_{(x,y)} : (x,y)\in R_i\right\}\middle|\alpha_i\right)\right) + \lambda\right), \tag{2}$$

where μ is a weight, ∂R_i is the boundary of the region R_i, and $P\left(I\left|\alpha_i\right.\right)$ is the pre-specified posteriori probability density function with α_i standing for the parameters contained in these functions; for example, when P is a Gaussian distribution, the α_i are the mean and variance of the image intensity.

The first term in Eq. (2) is related to the length of the boundaries and serves as the internal energy to control the smoothness of the moving contour; the parameter μ controls the influence of this term – a large μ is favorable to merge small sub-regions and avoid over-segmentation. The second term calculates the cost of classifying the pixels to their current region, and serves as the external energy to attract the contours to the correct boundaries. The third term λ is a weight defined for each region R_i based on the image contents; for example, λ can be penalties related to the area of each region.

Eq. (2) presents a rigorous modeling for the multiphase segmentation, but complex operations are required to minimize it [30, 31]. To solve this problem, a region competition model was proposed in [20] as:

$$\frac{\partial \phi_i}{\partial t} = H_\varepsilon{}'\left(\phi_i\right)\left(e_i - \max_{H_\varepsilon{}'\left(\phi_j\right)>0,\, j\neq i}\left(e_j, e_i - 1\right)\right), \text{ with} \tag{3}$$

$$e_k = \log\left(p_k\right) + \gamma \operatorname{div}\left(\frac{\nabla \phi_k}{\left|\nabla \phi_k\right|}\right),\ i,k = 1,\cdots,N\ ,$$

where γ is the weight of the internal force used to control the smoothness of the contour – a larger γ corresponds to a smoother boundary, $H_\varepsilon{}'\left(x\right)$ is the first derivative of a differentiable function $H_\varepsilon\left(x\right)$ that is used to approximate the Heaviside step

function $H(x)$ defined as $H(x)=1$, for $x\geq 0$ and $H(x)=0$, for $x<0$; for example, $H_\varepsilon(x)$ can be defined as $H_\varepsilon(x)=\frac{1}{1+e^{-x/\varepsilon}}$ with ε being a small positive number, p_k is the probability of a pixel belonging to the *k*-th region and is calculated according to the probability density function $P(I|\alpha_k)$ in Eq. (2), ∇ is the gradient operator, and div is the divergence operator.

The motion of contours given by Eq. (3) depends on the competitions among the neighboring regions, which is reflected by the comparison between the logarithms of the probabilities. The regions to which the local pixels are most likely to belong will expand, while the other regions will retract. The condition for the maximum operator requires that only regions that are close enough can compete with each other; the additional term e_i-1 assures that if there is a vacuum between neighboring regions, a region will move forward and cover it. Thus, an image can be segmented completely without overlapping.

2.2.2 Prior shape knowledge

Prior shape information is a valuable cue for robust and efficient segmentation. To use the shape guidance, the difference between the current shape and the prior shape needs to be quantified. Based on the dissimilarity measure defined in [32, 33], an effective energy functional was proposed in [21] as:

$$E(\phi)=d^2(\phi,\phi_0)=\int_\Omega\left(H\left(\phi\left(x+\mu_\phi\right)\right)-H\left(\phi_0(x)\right)\right)^2 dx, \qquad (4)$$

where Ω is the image region, ϕ_0 is the level set function defined as the signed distance function to the prior shape, and $\mu_\phi = \int_\Omega xH(\phi)dx \Big/ \int_\Omega H(\phi)dx$ is the center of gravity of the area defined by the moving contour.

According to the Euler-Lagrange equation of Eq. (4), the equation of motion was derived as:

$$\frac{\partial \phi}{\partial t} = -\left(H\left(\phi(x)\right) - H\left(\phi_0\left(x-\mu_\phi\right)\right)\right) - \frac{\left(x-\mu_\phi\right)^T}{\int H(\phi)dx} \times \int \left(H\left(\phi(x')\right) - H\left(\phi_0\left(x'-\mu_\phi\right)\right)\right)\delta\left(\phi(x')\right)\nabla\left(\phi(x')\right)dx' \quad . \qquad (5)$$

Following Eq. (5), the contour will evolve until its shape matches the defined prior shape. Hence, the model provides a simple way to incorporate the shape guidance. However, the use of shape guidance normally works on the premise that the shape of the structure does not have large variations. However, the shapes of the pelvic organs are closely related to the patient's physiological status and have considerable variations among different individuals; therefore, no representative training set is available. Strategies are adopted in the proposed approach to use this cue for segmentation.

3. Methods

Due to the complex imaging background and the irregular shapes, it is difficult to define a region of interest (ROI) that covers the three pelvic organs in a simple background. Three level set functions were defined and coupled together to segment simultaneously the three pelvic organs: urinary bladder, vagina and rectum. Since these organs are near each other, initial contours were defined manually within the boundaries of each organ

in order to obtain the correct intensity distributions and exclude any influences among these organs and from their neighboring structures, such as the obturator internus muscles. Hence, the segmentation is accomplished through the expansion of the initial contours.

To facilitate the following discussion, the level set function ϕ_1 is used to segment the bladder, ϕ_2 for the vagina, and ϕ_3 for the rectum. All the initial level set functions are defined as the signed distance functions with positive (negative) values inside (outside) the contour. Correspondingly, the internal region of the moving contour i at the time t is $\Omega_i = \{(x, y) | \phi_i(x, y, t) \geq 0\}$, with $i = 1, 2, 3$.

3.1 Bladder

As discussed in Section 2.1, the bladder can have large shape variations even in the same image series. Hence, no prior shape information is available. Additionally, the imaging appearances of the bladder can vary largely due to the inhomogeneous magnetic field. Segmentation only through the intensity or the intensity gradient is not reliable. However, given the different appearances of the pelvic organs and the appearance of the bladder wall, if the initial contours are placed inside the bladder lumen and expand according to the local intensity similarity, they will stop at the bladder wall. Hence, the region competition model in Eq. (3) can be used to segment the bladder. Since the three initial contours are all inside the organs and the organs are spatially next to each other, the gaps between the pelvic organs should not be covered by the moving contours. Therefore, the term $e_1 - 1$ in the maximum operator of Eq. (3) should be removed and the equation of motion for segmenting the bladder should be:

$$\frac{\partial \phi_1}{\partial t} = \delta(\phi_1)\left(e_1 - \max(e_2, e_3) + \gamma \mathrm{div}\left(\frac{\nabla \phi_1}{|\nabla \phi_1|} \right) \right), \tag{6}$$

where $e_k = \log(p_k)$, $k = 1, 2, 3$.

Nevertheless, there are still problems when using the above equation of motion. To clarify this point, supposing the intensity distribution of the pelvic organs can be described by the Gaussian functions and $e_2 \geq e_3$, then the external force is:

$$e_1 - \max(e_2, e_3) = -\frac{1}{2}\left(\frac{1}{\sigma_1^2} - \frac{1}{\sigma_2^2} \right) I^2 + \left(\frac{u_1}{\sigma_1^2} - \frac{u_2}{\sigma_2^2} \right) I - \frac{1}{2}\left(\frac{u_1^2}{\sigma_1^2} - \frac{u_2^2}{\sigma_2^2} \right) + \log\left(\frac{\sigma_2}{\sigma_1} \right),$$

where u_i and σ_i are the mean and standard deviation of the intensity, respectively.

For the sake of simplicity, if one considers $\sigma_1 = \sigma_2 = \sigma$, then the above formula becomes:

$$e_1 - \max(e_2, e_3) = \frac{u_1 - u_2}{\sigma^2}\left(I - \frac{u_1 + u_2}{2} \right).$$

As the mean intensity of the bladder region is highest among the three pelvic organs ($u_1 > u_2$), the speed function in Eq. (6) is an increasing function of the image intensity I when $I > \frac{u_1 + u_2}{2}$. However, the relationship between the probability p_1 and the contour movement is unclear. For example, if the contour arrives at the pixels with intensity $I > u_1 + 3\sigma_1$, which means p_1 is small and the contour is probably moving outside the bladder region, the contour will still move forward with a speed greater than

the ones at the pixels with intensity $|I-u_1|<3\sigma_1$. This is undesirable as the moving contour is supposed to stop at the bladder boundary.

According to Eq. (3), an image can be segmented completely and the contours stop at the boundaries of the regions. While here the appearance comparison is only among the three pelvic organs, in some images the appearances of the perivesical tissues and fats are more similar to the bladder compared with the other two organs; then, the speed calculated by Eq. (6) may still be large, even if the value of p_1 is small. If the bladder wall is blurred, when the contour moves there, the large speed of expansion will make the contour leak into the surrounding tissues and cannot be pulled back. A case in point is shown in Fig. 3. The relationship between p_1 and the speed of expansion is shown in Fig. 3c by using the scatter diagram of the pixels inside a neighboring band (r = 10) around the bladder boundary. One can see that with the maximum operator and logarithmic operations involved, the speeds can be quite different even if the values of p_1 are similar; and when p_1 is small, the speed value does not decrease much.

Thus, the good properties of the region competition model in Eq. (3) cannot be used for the local segmentation. To solve these problems, the equation of motion is proposed as:

$$\frac{\partial \phi_1}{\partial t}=\delta(\phi_1)\left(p_1\left(e_1-\max\left(e_2,e_3,e_1-1\right)\right)+\alpha\nabla p_1\cdot\nabla\phi_1+\gamma_1\mathrm{div}\left(\frac{\nabla\phi_1}{|\nabla\phi_1|}\right)\right), \qquad (7)$$

where δ is the Dirac delta function, $p_i=\frac{1}{\sqrt{2\pi}\sigma_i}\exp\left(-\frac{(I-u_i)^2}{2\sigma_i^2}\right)$ and $e_i=\log(p_i)$, u_i and σ_i are the mean and the standard deviation of the intensity inside the moving

contour i, with $i=1,2,3$, α is the weight to control the influence of the probability gradient field and γ_1 is the weight to control the influence of the internal force.

[insert Fig. 3 about here]

Compared with Eq. (3), the region competition by Eq. (7) does not require that the regions in competition are very close to each other; and the first term is multiplied by the probability p_1. As $p_1\left(e_1-\max\left(e_2,e_3,e_1-1\right)\right)\to 0$ when $p_1\to 0$, the multiplication guarantees that the contour will slow down when it arrives at the bladder boundary where p_1 becomes small. In the maximum operator, the term e_1-1 has a different role to the one in Eq. (3): it was used to keep the speed of expansion between 0 (zero) and 1 (one) so as to facilitate the selection of parameters and make the movement stable. The second term $\nabla p_1\cdot\nabla\phi_1$ can attach the contour to the bladder boundary, which was derived from $\nabla g\cdot\nabla\phi_1$ in the geodesic active contours by replacing the gradient-based function $g\left(I\right)$ with the region-based probability function $p_1\left(I\right)$. The replacement makes the calculation not only related to the neighboring pixels, but also depends on the intensity statistics of the whole bladder region. Therefore, the movement becomes less sensitive to intensity variations.

3.2 Vagina and rectum

When the images are appreciably influenced by noise, the vagina and the rectum cannot be segmented merely based on their imaging appearances. As such, shape guidance is

critical for the segmentation of the two organs. In fact, a shape constraint can help the moving contours pass the unwanted inner boundaries and also avoid leakages.

However, in a patient-specific study the prior shape knowledge of the vagina and the rectum is not always available before segmentation. Besides, for different individuals, the two pelvic organs can have large shape variations depending on their ages, conditions and physiological status. These features imply that advanced techniques for incorporating prior shape constraints are not suitable for this application. In the segmentation of the vagina and the rectum, the algorithm introduced in Section 2.2.2 was adopted, which is a simple and straightforward way to incorporate a shape constraint. It should be noted that even if the prior shape is not accurate, the force based on the shape constraint can help the contours pass the unwanted inner boundaries and avoid leakages.

3.2.1 Vagina

The appearance of the vagina can be easily distorted by noise, and the different layers have distinct appearances in T2-weighted MR images. Hence, besides handling the influence of noise, the external forces should assure the bypass of the unwanted inner boundaries and drive the contour to the outer boundary.

As the shape of the vagina normally does not exhibit dynamic changes in the axial plane in the same image series, prior shape knowledge can be integrated to assist the segmentation. Meanwhile, given the different appearances between the organs and the surrounding tissues, the equation of motion to segment the vagina is proposed as:

$$\frac{\partial \phi_2}{\partial t} = \delta(\phi_2)\left(p_2\left(e_2 - \max\left(e_1, e_3, e_2 - 1\right)\right) + \beta S_v + \gamma_2 \mathrm{div}\left(\frac{\nabla \phi_2}{|\nabla \phi_2|}\right)\right), \quad (8)$$

where δ, p_2, e_1, e_2, and e_3 are defined as in Eq. (7), β is the weight to control the influence of the shape constraint, γ_2 is the weight used to control the effect of curvature in order to smooth the moving contour, and:

$$S_v = -\left(H\left(\phi_2(x)\right) - H\left(\phi_v\left(x - \mu_{\phi_2}\right)\right)\right) - \frac{\left(x - \mu_{\phi_2}\right)^T}{\int H\left(\phi_2\right) dx} \times \int \left(H\left(\phi_2(x')\right) - H\left(\phi_v\left(x' - \mu_{\phi_2}\right)\right)\right) \delta\left(\phi_2(x')\right) \nabla \phi_2(x') dx',$$

with the level set function ϕ_v being the signed distance function to the prior shape of the vagina, and the remaining items are defined as in Eq. (4).

In order to avoid leakage, the first term is multiplied by the probability p_2; also the additional term $e_2 - 1$ in the maximum operator is used to keep the movement stable. The final status of the moving contour by Eq. (8) is determined by two forces: one is from the imaging appearance and the other is from the prior shape knowledge. The guidance provided by the prior shape is necessary to obtain the correct boundary when the continuity of the vagina boundary is interrupted by noise or when the multiple layers are clearly presented in the images.

Due to the distinct appearances of the layers, the mean intensity u_2 and the standard deviation σ_2 of the vagina region should be calculated carefully. Otherwise, the values may become larger due to the high signal intensity of the central strip, which can affect the appearance comparison and lead to incorrect segmentation results. To solve this

problem, the initial contours should be placed inside the vaginal wall so that the bright central strip of the vagina will not be covered; and u_2 and σ_2 are calculated in the subset of Ω_2 defined as:

$$\Omega_2^* = \Omega_2 \cap \left\{ (x,y) \middle| p_2(x,y) > p_1(x,y), p_3(x,y) \right\}. \quad (9)$$

This subset Ω_2^* excludes the high signal intensity pixels of the vaginal canal and the secretion. Hence, possible confusions caused by the miscalculation of the intensity statistics can be avoided.

3.2.2 Rectum

Like the vagina, the different layers of the rectum can be identified in T2-weighted MR images; therefore, the segmentation algorithm should be able to handle the influences of inhomogeneous intensities and assure the bypass of the inner rectal wall, and so the equation of motion is proposed as:

$$\frac{\partial \phi_3}{\partial t} = \delta(\phi_3)\left(\max(p_2, p_3) \cdot \left(e_3 - \max(e_1, e_3 - 1)\right) + \nu S_r + \gamma_3 \mathrm{div}\left(\frac{\nabla \phi_3}{|\nabla \phi_3|} \right) \right), \quad (10)$$

where δ, e_1, e_3, p_2, and p_3 are defined as in Eq. (7), ν and γ_3 are the weights with the same function as β and γ_2 in Eq. (8), and:

$$S_r = -\left(H(\phi_3(x)) - H\left(\phi_r\left(x - \mu_{\phi_3}\right)\right)\right) - \frac{\left(x - \mu_{\phi_3}\right)^T}{\int H(\phi_3)\,dx} \times \int \left(H(\phi_3(x')) - H\left(\phi_r\left(x' - \mu_{\phi_3}\right)\right)\right) \delta(\phi_3(x')) \nabla \phi_3(x')\,dx',$$

with the level set function ϕ_r representing the signed distance function to the prior shape of the rectum.

Due to the similarity between the appearances of the rectal lumen and the vaginal wall, the terms in the maximum operator are changed to $\max(e_1, e_3 - 1)$. Therefore, the comparison is only between the bladder and the rectum. To avoid leakage the first term is multiplied by $\max(p_2, p_3)$ instead of p_3, so that the contour will not stop at the rectal lumen where p_3 is small but where p_2 is large. Compared with the bladder, the appearance of the rectal lumen is more similar to the rectal wall; hence, the contour can pass the inner boundary according to Eq. (10).

Likewise, due to the distinct appearances of the rectal layers, most parts of the initial contour should be placed inside the rectal wall, and the mean intensity u_3 and the intensity standard deviation σ_3 are calculated in the subset of Ω_3 defined as:

$$\Omega_3^* = \Omega_3 \cap \left\{ (x, y) \middle| p_3(x, y) > p_1(x, y), p_2(x, y) \right\}. \quad (11)$$

The subset Ω_3 excludes the pixels of the rectal lumen, and therefore avoids any possible confusion caused by their similar appearances to the vaginal wall. Otherwise, the mean intensity u_3 of the rectum can be close to the mean intensity u_2 of the vagina, which may affect the appearance comparison and lead to an incorrect segmentation.

3.3 Parameters and external forces

Initial contours need to be placed inside the boundary of each organ properly as aforementioned. Their locations can affect the results of segmentation, and the incorrect

appearance comparison may lead to wrong segmentations: for the bladder, the initial contours should avoid the highly inhomogeneous regions; for the vagina and the rectum, the initial contours should be placed so that their main parts are outside the vaginal canal and the rectal lumen.

The parameters γ_i with $i = 1, 2, 3$ in the equations of motion control the influence of the internal forces; a larger value can lead to a smoother boundary. The parameter α determines the weight of the gradient field of the probability which is used to accelerate the curve evolution and prevent leakage. Compared with the weights of the shape constraint, the four parameters only have minor influences on the segmentation and therefore can be selected easily; their values are usually fixed when processing images from the same image series.

Given that the final boundaries are obtained under two external forces, the prior shape does not need to be accurate. With an inaccurate prior shape, the force derived from the prior shape energy can make the contour pass the possible local boundaries caused by noise or intensity variation. Then, once the boundaries in an image are correctly segmented, they are used as the prior shapes for the sequential slices, and the prior shape can be refined by averaging the obtained contours as suggested in [32]. The two external forces derived from the prior shape and the appearance comparison need to be well balanced. As the shapes of pelvic organs can vary in different slices, the main external force is the one derived from the appearance comparison. Hence, the influence of appearance comparison is normally larger than the one of shape constraint. Nevertheless, if the images are severely distorted by noise or PVE, the influence of shape constraint should be increased so that the moving contours can be guided to the

correct boundary. Therefore, the proper values of the weights β and ν are related to the image quality.

When the prior shapes of the vagina and rectum are unavailable, a rectangle can be used as an approximate shape of the vagina and a circle for the rectum on the axial MR images. Then once the boundaries in an image are segmented correctly, they are used as the prior shapes to assist the segmentation of the sequential slices; also, the approximate shapes can be refined by the method suggested in [32].

3.4 Intensity statistics

The intensity statistics of the three pelvic organs are updated along with the evolution of the moving contours. In the beginning phase, these values are obtained from local areas and may deviate from the ground truth. Imprecision can lead to miscalculation of the probability and cause dynamic changes of the speed function, which may affect the contour movement and lead to wrong results. To avoid this, the standard deviation is computed as $\sigma_i = \max(\sigma_i, \sigma_0)$, with $i = 1, 2, 3$, where σ_0 is a predefined value. Then, if σ_1 , σ_2, and σ_3 are smaller than σ_0, the standard deviation of the intensity inside each region is assumed to be equal. The appearance comparison in the proposed approach is actually the comparison between the magnitudes of $|I - u_i|$, with $i = 1, 2, 3$, which is the difference between the intensity of a pixel and the mean intensity of each region, a similar segmentation path as used in the k-means algorithm [35]. The value of σ_0 is also related to the image qualities; a larger σ_0 means a wider range in which the intensities of the pelvic organs are allowed to vary. The modification makes the segmentation less sensitive to the initial conditions and more flexible to handle the inhomogeneous intensities.

However, since the dimensions of the pelvic organs are not equal, one or two organs may not be present in some images in an image series. In this case, the strategy adopted was that once the pelvic organs are segmented in an image, the intensity statistics of each organ are stored. As such, if one or two organs are missing in the neighboring images, the stored statistical information is used.

3.5 Outline of the novel approach

The coupling approach changed the region competition algorithm in [20] into a new algorithm that can handle the segmentation of local image regions with the assistance of shape constraints. To conclude, the proposed approach that integrates the three geometric deformable models is:

$$\begin{cases} \dfrac{\partial \phi_1}{\partial t} = \delta(\phi_1)\left(p_1\left(e_1 - \max\left(e_2, e_3, e_1 - 1\right)\right) + \alpha \nabla p_1 \cdot \nabla \phi_1 + \gamma_1 \mathrm{div}\left(\dfrac{\nabla \phi_1}{|\nabla \phi_1|}\right)\right) \\ \dfrac{\partial \phi_2}{\partial t} = \delta(\phi_2)\left(p_2\left(e_2 - \max\left(e_1, e_3, e_2 - 1\right)\right) + \beta S_v + \gamma_2 \mathrm{div}\left(\dfrac{\nabla \phi_2}{|\nabla \phi_2|}\right)\right) \\ \dfrac{\partial \phi_3}{\partial t} = \delta(\phi_3)\left(\max\left(p_2, p_3\right) \cdot \left(e_3 - \max\left(e_1, e_3 - 1\right)\right) + \nu S_r + \gamma_3 \mathrm{div}\left(\dfrac{\nabla \phi_3}{|\nabla \phi_3|}\right)\right) \end{cases}, \quad (12)$$

where the level set function ϕ_1 is used to segment the bladder, ϕ_2 is used to segment the vagina and ϕ_3 is used to segment the rectum. To further decrease the influence of noise, the intensity of a pixel $I(X_0)$ is changed to the average intensity of its *m*-connected neighbor set $N_m(X_0)$ as $\bar{I}(X_0) = \dfrac{1}{|N_m(X_0)|}\sum_{X \in N_m(X_0)} I(X)$; or one can choose to replace the probability $p_i(X_0)$ with the joint probability $\prod_{X \in N_m(X_0)} p_i(X)$ as used in

[30]. The initial contours need to be correctly defined inside the organ regions as stated in Section 3.3.

The proposed procedure can be summarized into the following three steps, and the application of the narrow band method [34] is used to improve the computational efficiency:

0. *Preprocessing*: Smooth the input image using a Gaussian kernel.

1. *Initialization:* Set $t = 0$, place the initial contours inside the organ regions and

(a) Build the level set functions ϕ_v and ϕ_r according to the prior shapes of the vagina and the rectum;

(b) For each organ, define a narrow band around each initial contour; and initialize the level set functions $\phi_i(x, y, 0)$ using the signed distance function, with $i = 1, 2, 3$;

(c) Calculate the mean u and the standard deviation σ of the intensity distributions of the region Ω_1, Ω_2^* and Ω_3^*.

2. *Iteration*: Set $t = t + 1$, update the level set values according to Eq. (12). Then update the values of u and σ for each region.

3. *Judgment:* Check whether the contours have stopped moving or whether the iteration time has reached a maximum threshold, i.e. $t > T_{threshold}$ (in this situation the contour movements are considered to be stopped). If neither case is true, return to Step 2; otherwise, stop the iteration process.

4. Experiments

Two image series are used here to illustrate the performance of the proposed approach. One was acquired from a symptomatic 63-year-old multiparous woman under a turbo-spin echo (TSE) sequence with a field strength of 1.5 T, TE: 103 ms, TR: 5230 ms, and an acquisition matrix of 320×272. This axial image series contains 28 image slices, and the spatial resolution of the axial images is 0.69×0.69×5.40 mm3. The other image series was from an asymptomatic nulliparous 20-year-old woman under a TSE sequence with a field strength of 1.5 T, TE: 98 ms, TR: 3980 ms, and an acquisition matrix of 320×192. This axial image series contains 40 image slices, and the spatial resolution of the axial images is 1.00×1.00×5.400 mm3.

The two image data were chosen because they are suitable and representative to show the imaging features of the three pelvic organs on the axial MR images. Fig. 4 illustrates nine images of the two series; on these images the different shapes of the bladder at different imaging positions and between individuals can be clearly seen; the distinct layers of the vagina can be seen on the images acquired from the younger woman, and the different layers of the rectum can be seen better on the images from the older woman. The initial contours were defined inside the pelvic organs following the rules defined in Section 3.3; then, the segmentation was carried out through the procedures summarized in Section 3.5. When processing the images acquired from the elder woman, a rectangle of the dimensions equal to 5×70 (pixel size) was used as the prior shape of the vagina and a circle with radius equal to 18 (pixel size) was used for the rectum. For the images illustrated in Fig. 4, the parameters chosen were $\alpha = 0.1$, $\nu = 1$, $\gamma_i = 1$ with $i = 1, 2, 3$, $\beta = 0.5$ in Figs. 4(d)-(f) and $\beta = 1$ in the remaining ones.

To evaluate the segmentation results, the ground truth was obtained through averaging the manual segmentations performed separately by three experienced technicians, as proposed in [32]. Then, the boundaries segmented by the proposed algorithms (red contours) were overlapped with the ground truth (green contours) so that the deviations could be clearly depicted.

[insert Fig. 4 about here]

Despite the presence of noise and the PVE, the bladders were correctly segmented by the proposed solution. In Figs. 4(a)-(c), the central high signal intensity strip of the vagina is almost invisible and the whole vagina region appears as a thin band with a blurred boundary due to the PVE. On the other hand, by adopting the proposed external forces, the moving contour kept the integrity and arrived at the correct boundary. In Figs. 4(d)-(f), the images are of the upper third of the vagina, near to the cervix, and this part is rounder and narrower in appearance than the lower two thirds. Although the prior shape used was not accurate, the correct boundaries were still segmented. In Figs. 4(g)-(i), the distinct layers of the vagina are observed more clearly; with the proposed solution, the moving contour passed the central high intensity strip and successfully arrived at the outer boundary. Likewise, the layers of the rectum are easily observed in the images. The inner boundary that enclosed the rectal lumen was passed by, and the outer boundaries were correctly segmented.

To quantitatively evaluate the segmentation results, the Hausdorff distance was adopted. Supposing C_0 is the true boundary and C_1 is the contour segmented by the proposed algorithm, the Hausdorff distance is calculated as:

$$D(C_0, C_1) = \max\left(\max_{p \in C_0} D(p, C_1), \max_{p \in C_1} D(p, C_0)\right), \tag{13}$$

where the point-to-contour distance was defined as:

$$D(p, C) = \min_{p_1 \in C} d(p, p_1), \tag{14}$$

and $d(p, p_1)$ is the Euclid distance between two points.

In addition, a measure similar to the average symmetric absolute distance error was used to check the overall point-to-point matching between the two contours:

$$AD(C_0, C_1) = \left(MD(p, C_0) + MD(p, C_1)\right) / 2, \tag{15}$$

where $MD(p, C_0)$ is the average value of the distances $D(p, C_0)$ for point $p \in C_0$ and $MD(p, C_1)$ is the average value of the distances $D(p, C_1)$ for point $p \in C_1$.

Table 1 shows the comparative results of the images illustrated in Fig. 4. Considering the spatial resolution of the image data, the average deviation from the ground truth is around 1 to 2 pixels. The average Hausdorff distance and the average symmetric distance for the illustrated two image series are shown in Table 2. One can see with the coupling approach the segmentation is not much affected by the noise and PVE. The obtained boundaries are promising both qualitatively and quantitatively.

[insert Table 1 about here]

[insert Table 2 about here]

Table 3 presents the intensity statistics of the three pelvic organs in the images of Fig. 4. Based on the values indicated, the large variances of intensity in the vagina and rectum can be verified. The values listed in parentheses are the ones calculated in the subsets Ω_2^* and Ω_3^* defined in Eqs. (9) and (11), respectively; the differences between the values reflect the different intensity distributions of the organs, and these differences also support the reason why u_i and σ_i, with $i = 2,3$, should be calculated in these subsets.

[insert Table 3 about here]

6. Conclusion

The novel geometric deformable models proposed in this paper can effectively handle the segmentation of pelvic organs in axial T2-weighted MR images. The different appearances between the organs and the prior shape knowledge are incorporated into a level set framework. The coupling between the moving contours is achieved through the intensity statistics of the three pelvic organs. The three pelvic organs can be segmented simultaneously, and with shape constraints the approach is less sensitive to the influence of noise and partial volume effect.

The satisfactory performance of the coupling approach is based on the premises that the initial contours are defined properly, the acquired MR image data are not severely influenced by noise or partial volume effect, and the shapes of the vagina and the rectum are not seriously deformed. Therefore, the proposed computational approach may not be fully satisfactory in some cases; for example, when the pelvic organs have suffered considerable deformations due to injuries or when their appearances are severely distorted by noise. In addition, one may notice that the suggested solution requires that the three organs appear together in the input image. When this does not occur, intensity statistics from the images that have been processed can be used to compensate the missing information, but the performance of the approach may be affected. Fig. 5 illustrates two images in which applying the coupling approach cannot obtain an ideal segmentation: in Fig. 5(a) additional information from other images is required to implement the coupling approach owing to the absence of urinary bladder; in Fig. 5(b), the statistics of intensity distribution inside the bladder lumen is considerably affected by the central dark area; therefore, without proper user intervention, the proposed approach will lead to incorrect segmentation.

[insert Fig. 5 about here]

As the proposed approach is based on deformable models, the parameters should be chosen suitably. Nevertheless, a fully automatic segmentation approach will be an even more valuable tool for medical applications, such as pelvic radiotherapy [36]. Hence, the future work aims to enhance the robustness and automation of the proposed

approach and for that, the integration of available anatomical statistics, such as incorporating the distance between different structures or the anatomical atlas can be a potential solution. Also, algorithms that correct the inhomogeneity on the original MR images, such as the ones proposed in [37, 38], can be useful to improve the performance and robustness of the segmentation and facilitate the selection of parameters.

Conflict of interest statement

None Declared.

Acknowledgements

This work was partially done in the scope of the projects “Methodologies to Analyze Organs from Complex Medical Images – Applications to Female Pelvic Cavity”, “Aberrant Crypt Foci and Human Colorectal Polyps: mathematical modeling and endoscopic image processing” and “Cardiovascular Imaging Modeling and Simulation - SIMCARD”, with references PTDC/EEA-CRO/103320/2008, UTAustin/MAT/0009/2008 and UTAustin/CA/0047/2008, respectively, financially supported by Fundação para a Ciência e a Tecnologia (FCT), in Portugal.

The first author would like to thank FCT for his PhD grant with reference SFRH/BD/43768/2008.

References

[1] V.L. Handa, T.A. Harris, D.R. Ostergard, Protecting the pelvic floor: obstetric management to prevent incontinence and pelvic organ prolapse, Obstet. Gynecol. 88 (1996), pp. 470-478.

[2] G.M. Buchsbaum, E.E Duecy, L.A. Kerr, L.S. Huang, D.S. Guzick, Urinary incontinence in nulliparous women and their parous sisters, Obstet. Gynecol. 106 (2005), pp. 1253-1258.

[3] E. Hutchinson, Constipation and the pelvic floor, Nat. Rev. Gastroenterol. Hepatol. 7 (2010), pp. 185-185.

[4] J.A. Fantl, D.K. Newman, J. Colling, et al. Urinary incontinence in adults: acute and chronic management. Clinical Practice Guideline, Clinical Practice Guideline, Rockville (MD): Agency for Health Care Policy and Research, Public Health Service, U.S. Department of Health and Human Services, No. 2. 1996.

[5] A.L. Olsen, V.J. Smith, J.O. Bergstrom, J.C. Colling, A.L. Clark, Epidemiology of surgically managed pelvic organ prolapse and urinary incontinence, Obstet. Gynecol. 89 (1997), pp. 501-506.

[6] S. Herschorn, Female pelvic floor anatomy: the pelvic floor, supporting structures, and pelvic organs, Rev. Urol. 6 (2004), pp. S2-S10.

[7] R.U. Margulies, Y. Hsu, R. Kearney, T. Stein, W.H. Umek, J.O. DeLancey, Appearance of the levator ani muscle subdivisions in magnetic resonance images, Obstet. Gynecol. 107 (2006), pp. 1064-1069.

[8] S. Paramasivam, A. Proietto, M. Puvaneswary, Pelvic anatomy and MRI, Best Pract. Res. Cl. Ob. 20 (2006), pp. 3-22.

[9] C. Klessen, P. Rogalla, M. Taupitz, Local staging of rectal cancer: the current role of MRI, Eur. Radiol. 17 (2007), pp. 379-389.

[10] K.F. Noakes, I.P. Bissett, A.J. Pullan, L.K. Cheng, Anatomically realistic three-dimensional meshes of the pelvic floor & anal canal for finite element analysis, Ann. Biomed. Eng. 36 (2008), pp. 1060-1071.

[11] F. Alexandre, R. El Sayed, T. Mascarenhas, R.N.M Jorge, M.P. Parente, A.A. Fernandes, J.M.R.S. Tavares, 3D reconstruction of pelvic floor for numerical simulation purpose, First ECCOMAS Thematic Conference on Computational Vision and Medical Image Processing, Porto, Portugal, October 2007, pp. 359-362.

[12] D.C. Collier, S.S. Burnett, M. Amin, S. Bilton, C. Brooks, A. Ryan, D. Roniger, D. Tran, G. Starkschall, Assessment of consistency in contouring of normal-tissue anatomic structures, J. Appl. Clin. Med. Phys. 4 (2003), pp. 17-24.

[13] Z. Ma, J.M.R.S. Tavares, R.N.M. Jorge, T. Mascarenhas, A review of algorithms for medical image segmentation and their applications to the female pelvic cavity, Comput. Meth. Biomech. Biomed. Eng. 13 (2010), pp. 235-246.

[14] Z. Ma, R.M.N. Jorge, J.M.R.S. Tavares, A shape guided C–V model to segment the levator ani muscle in axial magnetic resonance images, Med. Eng. Phys. 32 (2010), pp. 766-774.

[15] M. Rousson, A. Khamene, M. Diallo, J.C. Celi, and F. Sauer, Constrained surface evolutions for prostate and bladder segmentation in CT images, Lecture Notes in Computer Science, 2005, Volume 3765/2005, pp. 251-260.

[16] D. Pasquier, T. Lacornerie, M. Vermandel, J. Rousseau, E. Lartigau, N. Betrouni, Automatic segmentation of pelvic structures from magnetic resonance images for

prostate cancer radiotherapy, Int. J. Radiation Oncology Biol. Phys. 68 (2007), pp. 592-600.

[17] C. Duan, Z. Liang, S. Bao, H. Zhu, S. Wang, G. Zhang, J. Chen, H. Lu, A coupled level set framework for bladder wall segmentation with application to MR cystography, IEEE Trans. Med. Imaging. 29 (2010) 903-915.

[18] N. Joshi, S. Bond, M. Brady, The segmentation of colorectal MRI images, Med. Image Anal. 14 (2010), pp. 494-509.

[19] R. Adams, L. Bischof, Seeded region growing, IEEE Trans. Pattern Anal. Mach. Intell. 16 (1994), pp. 641-647.

[20] T. Brox, J. Weickert, Level set segmentation with multiple regions, IEEE Trans. Image Process. 15 (2006), pp. 3213-3218.

[21] D. Cremers, S.J. Osher, S. Soatto, Kernel density estimation and intrinsic alignment for shape priors in level set segmentation, Int. J. Comput. Vision. 69 (2006), pp. 335-351.

[22] K.L. Moore, A.F. Dalley, Clinically Oriented Anatomy, 4th ed., Lippincott Williams & Wilkins, Baltimore, 1999.

[23] K.T. Barnhart, A. Izquierdo, E.S. Pretorius, D.M. Shera, M. Shabbout, A. Shaunik, Baseline dimensions of the human vagina, Hum. Reprod. 21 (2006), pp. 1618-1622.

[24] U. Zaspel, B. Hamm, Vagina, in: B. Hamm, R. Forstner (Eds.), MRI and CT of the Female Pelvis, Springer, Berlin Heidelberg New York, 2007.

[25] V. Caselles, R. Kimmel, G. Sapiro, Geodesic active contours, Int. J. Comput. Vision. 22 (1997), pp. 61-79.

[26] S.J. Osher, J.A. Sethian, Fronts propagating with curvature-dependent speed: algorithms based on Hamilton-Jacobi formulations, J. Comput. Phys. 79 (1988), pp. 12-49.

[27] T. McInerney, D. Terzopoulos, Deformable models in medical image analysis: A survey, Med. Image Anal. 1 (1996), pp. 91-108.

[28] W.J. Niessen, B.M. ter Haar Romeny, M.A. Viergever, Geodesic deformable models for medical image analysis, IEEE Trans. Med. Imaging. 17 (1998), pp. 634-641.

[29] D.L. Pham, C. Xu, J.L. Prince, A survey of current methods in medical image segmentation, Ann. Biomed. Eng. 2 (2000), pp. 315-338.

[30] S.C. Zhu, A. Yuille, Region competition: unifying snakes, region growing, and Bayes/MDL for multiband image segmentation, IEEE Trans. Pattern Anal. Mach. Intell. 18 (1996), pp. 884-900.

[31] Y.G. Leclerc, Constructing simple stable descriptions for image partitioning, Int. J. Comput. Vision. 3 (1989), pp. 73-102.

[32] M.E. Leventon, W.E.L. Grimson, O. Faugeras, Statistical shape influence in geodesic active contours, in: Proceedings of the 2000 IEEE Conference on Computer Vision and Pattern Recognition, IEEE Computer Society, South Carolina, USA, 2000, pp. 316-323.

[33] T. Riklin-Raviv, N. Kiryati, N. Sochen, Unlevel-sets: geometry and prior-based segmentation, in: T. Pajdla, J. Matas (Eds.), Proceedings of 8th European Conference on Computer Vision, 3024, Springer, Berlin Heidelberg, New York, 2004, pp. 50-61.

[34] D. Adalsteinsson, J.A. Sethian, A fast level set method for propagating interfaces, J. Comput. Phys. 118 (1995), pp. 269-277.

[35] S. Lloyd, Least squares quantization in PCM, IEEE Trans. Inform. Theory. 28 (1982), pp. 129-137.

[36] B. Haas, T. Coradi, M. Scholz, P. Kunz, M. Huber, U. Oppitz, L. André, V. Lengkeek, D. Huyskens, A. van Esch, R. Reddick, Automatic segmentation of thoracic and pelvic CT images for radiotherapy planning using implicit anatomic knowledge and organ-specific segmentation strategies, Phys. Med. Biol. 53 (2008), pp. 1751-1771.

[37] U. Bagci, J.K. Udupa, L. Bai, The role of intensity standardization in medical image registration, Pattern Recogn. Lett. 31 (2010), pp. 315-323.

[38] A. Madabhushi, J.K. Udupa, Interplay between intensity standardization and inhomogeneity correction in MR image processing, IEEE Trans. Med. Imaging. 24 (2005), pp. 561-576.

FIGURE CAPTIONS

Fig. 1 Axial view of pelvic cavity with the boundaries of the structures identified, from top to bottom: bladder (in red), vagina (in green), rectum (in blue), and the levator ani muscle (in purple).

Fig. 2 Segmentation results using the geodesic active contours algorithm: (a) with unclear inner layer of rectum; (b) with clear inner layer of rectum.

Fig. 3 Leakage caused by the equation of motion defined in Eq. (6): (a) the leaked contour; (b) the speed direction of a narrow band at the bladder boundary (in white: expanding regions, in black: retracting regions); (c) the scatter diagram of the pixels that are inside the neighboring band of the bladder boundary ($r = 10$), illustrating the relationship between the probability (horizontal axis) and the expanding speed values (vertical axis), with blue (red) marker stands for the pixels inside (outside) the boundary.

Fig. 4 Segmentation results by the proposed approach (red contours) overlapped with the ground truth (green contours); from top to bottom, the organs segmented in each image are: bladder, vagina, and rectum. (Images from (a) to (f) are from the older woman and images from (g) to (i) are from the younger woman.)

Fig. 5 Examples of cases in which an ideal segmentation may not be obtained by applying the coupled approach: (a) the urinary bladder is not presented in the image; (b) the intensity distribution of the bladder is affected considerably.

TABLES CAPTIONS

Table 1 Comparison between the boundaries segmented by the proposed approach and the ground truth (HD: Hausdorff distance; AD: the average symmetric absolute surface distance defined in Eq. (15))

Table 2 Average values of the metrics for the illustrated two image series (HD: Hausdorff distance; AD: the average symmetric absolute surface distance defined in Eq. (15))

Table 3 The mean and standard deviation of the intensity in Fig. 4 (SD: standard deviation, the values in parentheses were obtained by the proposed solution)

SUMMARY

Due to the complex anatomy of female pelvic cavity, the segmentation of pelvic structures is a challenging task. The work in this paper focuses on the segmentation of bladder, vagina and rectum in T2-weighted axial magnetic resonance (MR) images.

The distinct imaging appearances of the three pelvic organs are used as the segmentation cues, and a novel region competition model is proposed. Besides, prior shape knowledge of the vagina and rectum is incorporated into the new model to assist the segmentation, given that the layers of two organs have different imaging appearances and their boundaries are usually distorted by noise and partial volume effect. The proposed approach is composed of three coupled geometric deformable models that combine the anatomical relationship and the imaging appearances of the pelvic organs and surrounding tissues. Using the proposed approach, the three pelvic organs can be segmented simultaneously, and the influence of noise and partial volume effect is overcome.

Here, the proposed approach is explained and discussed in detail, including specific implementation issues and the equations of motion are defined. Additionally, experimental examples are illustrated and discussed. Also future work perspectives to enhance the robustness and automation of this new approach are pointed out.

Tables

Table 1 Comparison between the boundaries segmented by the proposed algorithms and the ground truth (HD: Hausdorff distance; AD: the average symmetric absolute surface distance defined in Eq. (15))

Fig. 4	Bladder		Vagina		Rectum	
	HD (mm)	AD (mm)	HD (mm)	AD (mm)	HD (mm)	AD (mm)
a	2.48	1.02	1.54	0.39	1.38	0.52
b	1.54	0.66	1.54	0.45	1.38	0.32
c	1.38	0.39	0.69	0.21	0.69	0.37
d	2.06	0.54	1.54	0.83	1.54	0.51
e	2.48	0.64	0.97	0.72	0.97	0.35
f	1.38	0.66	1.38	0.70	1.94	0.57
g	2.00	0.86	2.00	0.66	1.00	0.40
h	3.61	1.51	3.00	0.90	2.00	0.78
i	2.83	0.90	2.24	0.57	1.41	0.62

Table 2 Average values of the metrics for the illustrated two image series (HD: Hausdorff distance; AD: the average symmetric absolute surface distance defined in Eq. (15))

Series	Bladder		Vagina		Rectum	
	HD (mm)	AD (mm)	HD (mm)	AD (mm)	HD (mm)	AD (mm)
1	1.93	0.61	1.32	0.52	1.16	0.38
2	2.72	1.00	2.05	0.59	1.28	0.50

Table 3 The mean and standard deviation of the intensity in Fig. 4 (SD: standard deviation, the values in parentheses were obtained by the proposed solution)

Fig. 4	Bladder		Vagina		Rectum	
	Mean	SD	Mean	SD	Mean	SD
a	163.1	16.3	44.5 (40.9)	16.2 (9.1)	77.5 (77.7)	18.1 (13.2)
b	165.2	16.5	46.2 (41.6)	15.2 (6.9)	66.5 (69.1)	19.1 (17.7)
c	175.0	12.5	41.4 (40.1)	15.4 (9.8)	57.3 (65.4)	25.8 (16.3)
d	129.9	10.3	22.0 (21.2)	7.0 (4.5)	46.0 (47.0)	19.8 (17.2)
e	148.3	12.0	21.6 (21.1)	6.0 (3.5)	51.6 (55.1)	17.8 (15.1)
f	132.3	10.3	19.9 (19.2)	5.8 (3.6)	52.7 (43.7)	15.4 (11.4)
g	190.8	10.1	41.9 (43.8)	12.5 (6.0)	23.2 (28.1)	13.7 (12.0)
h	175.2	17.4	39.3 (39.8)	12.0 (5.4)	22.2 (15.0)	26.8 (10.2)
i	168.3	15.5	49.8 (53.9)	17.0 (14.5)	16.8 (11.7)	16.0 (3.9)

FIGURES

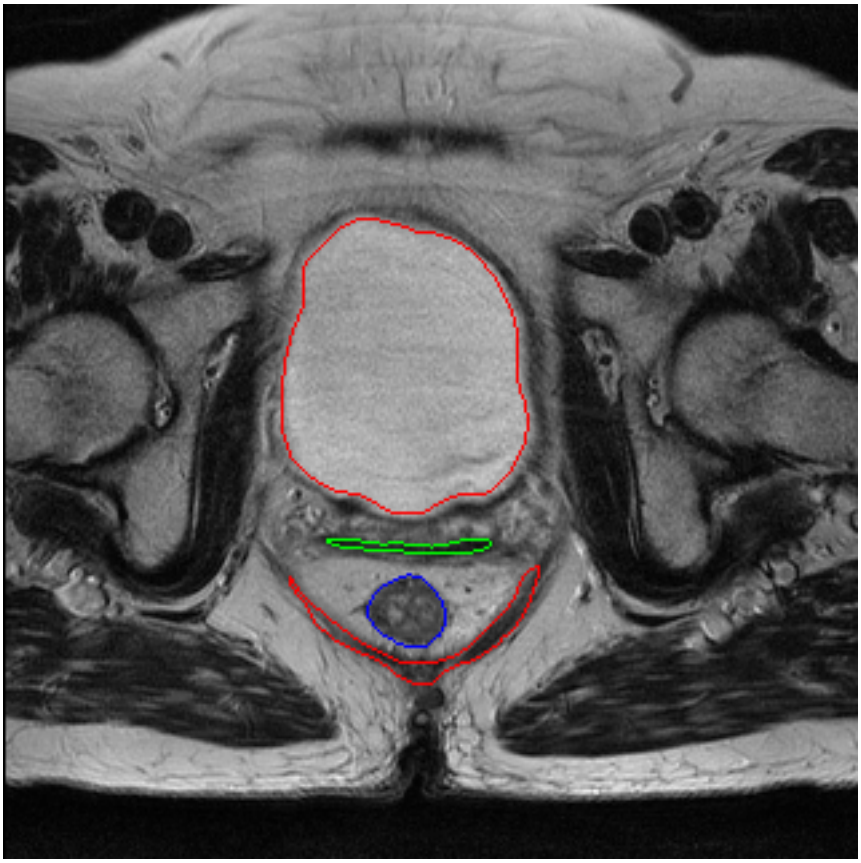

Figure 1

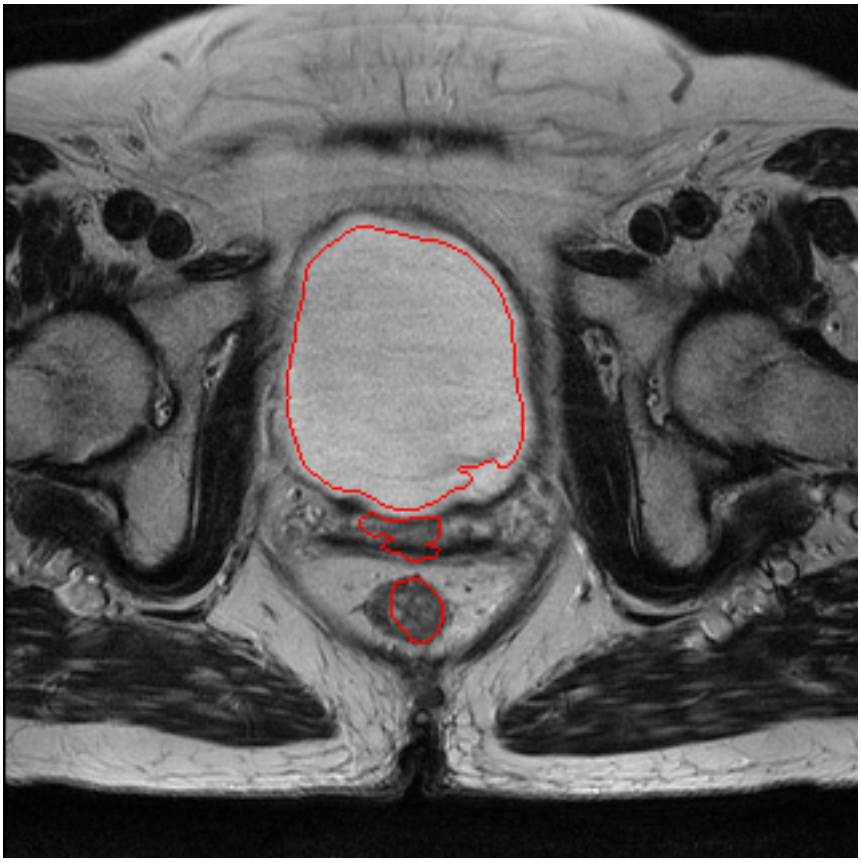

Figure 2a

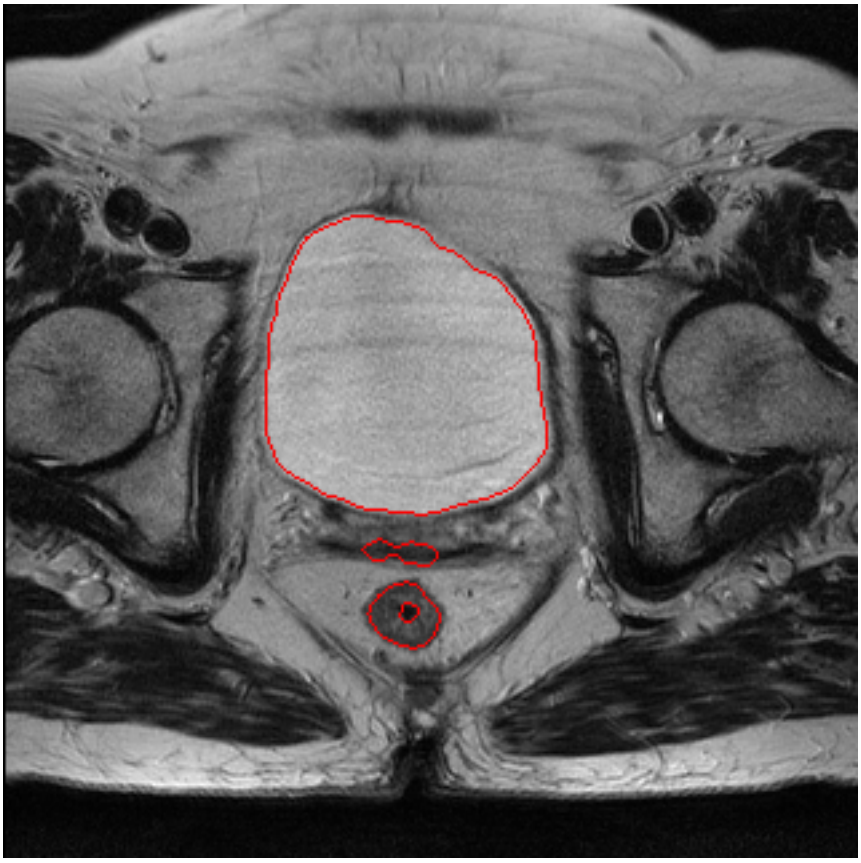

Figure 2b

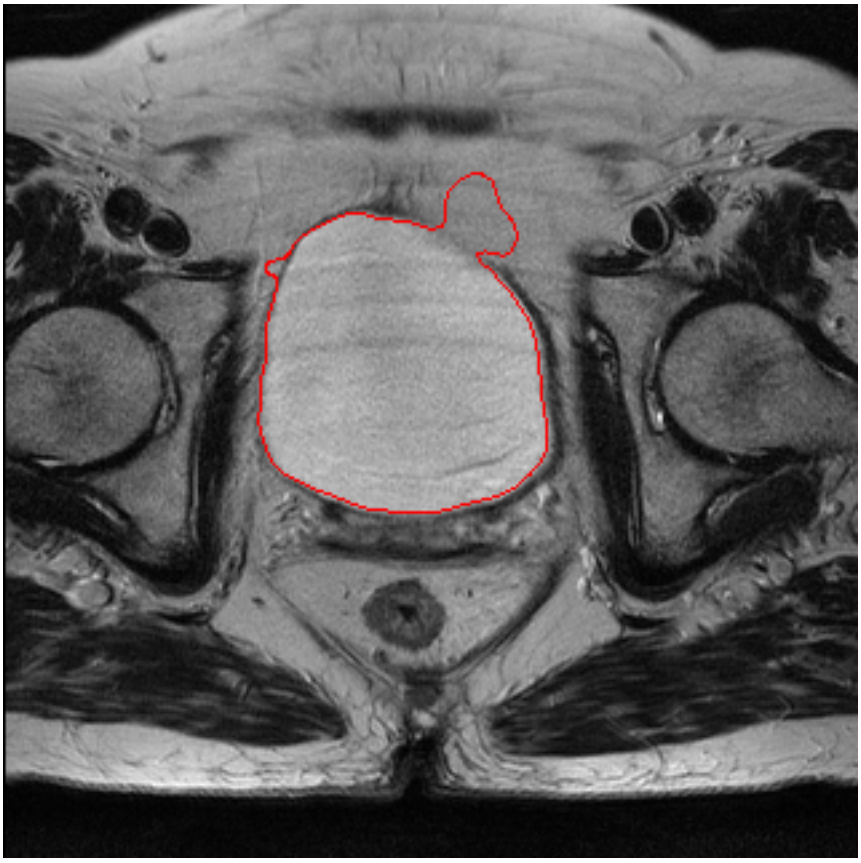

Figure 3a

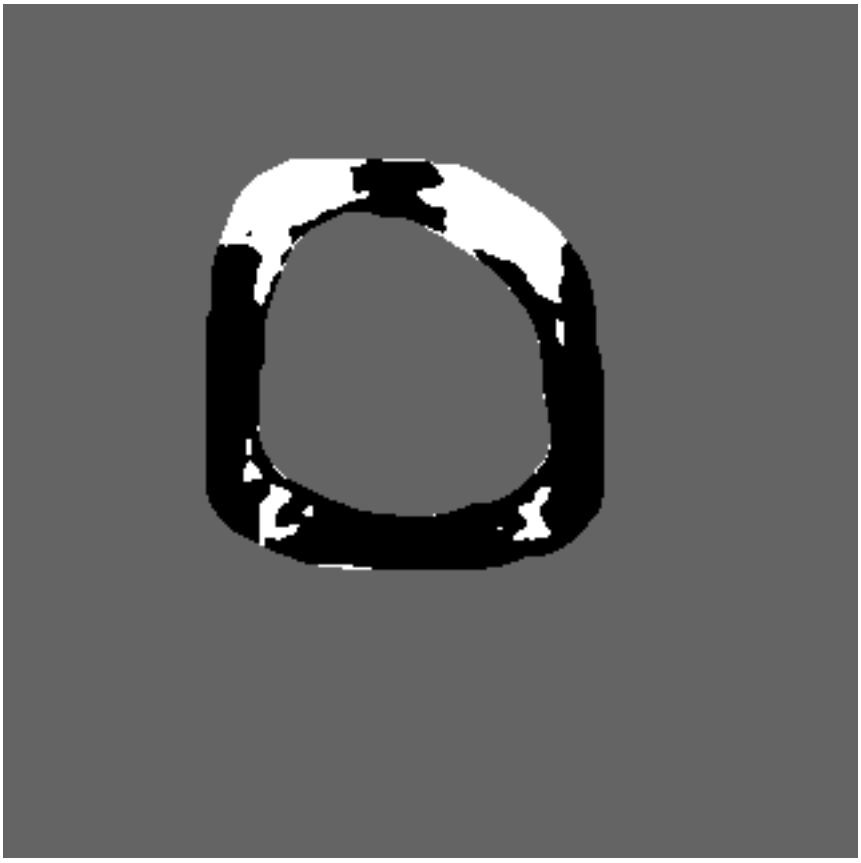

Figure 3b

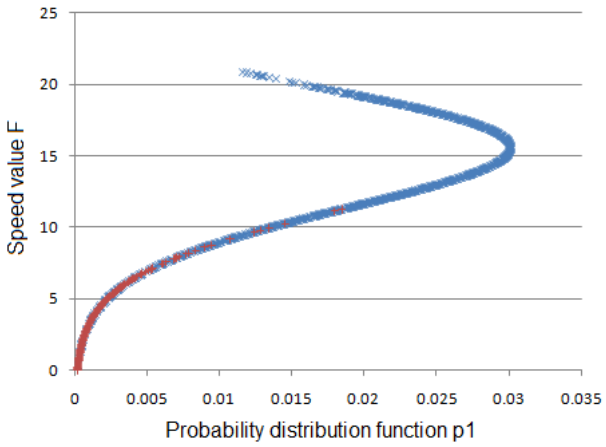

Figure 3c

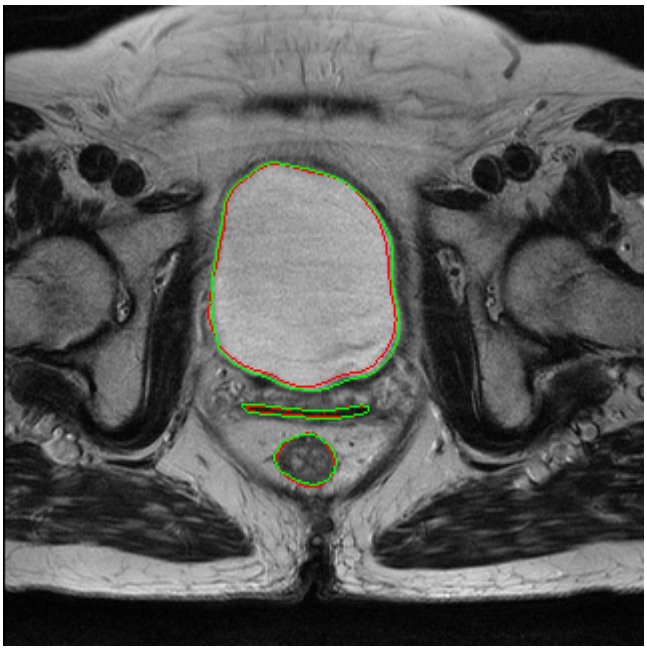

Figure 4a

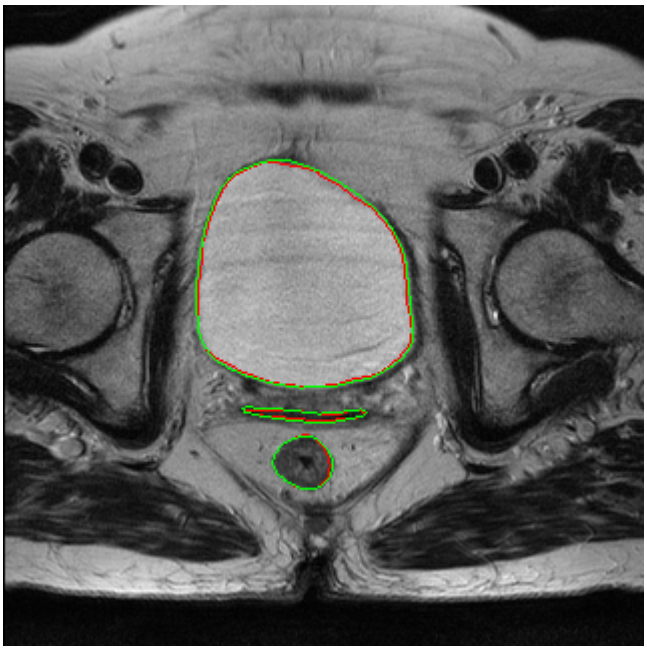

Figure 4b

Figure 4c

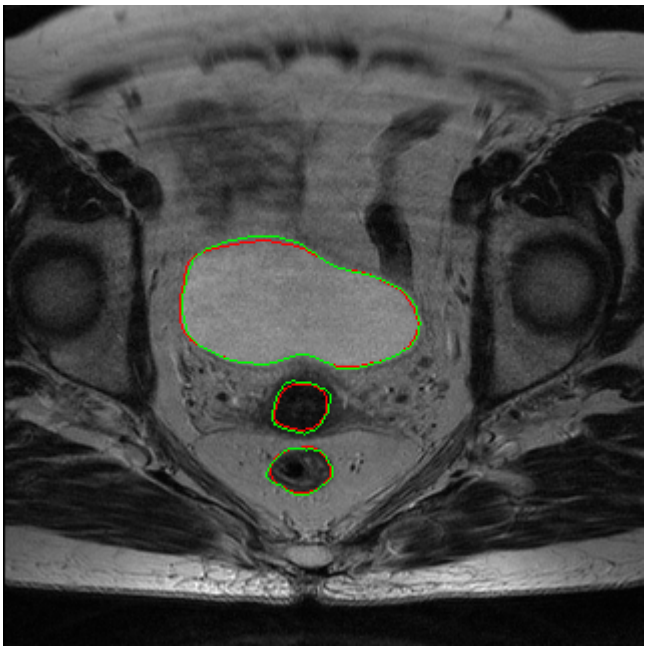

Figure 4d

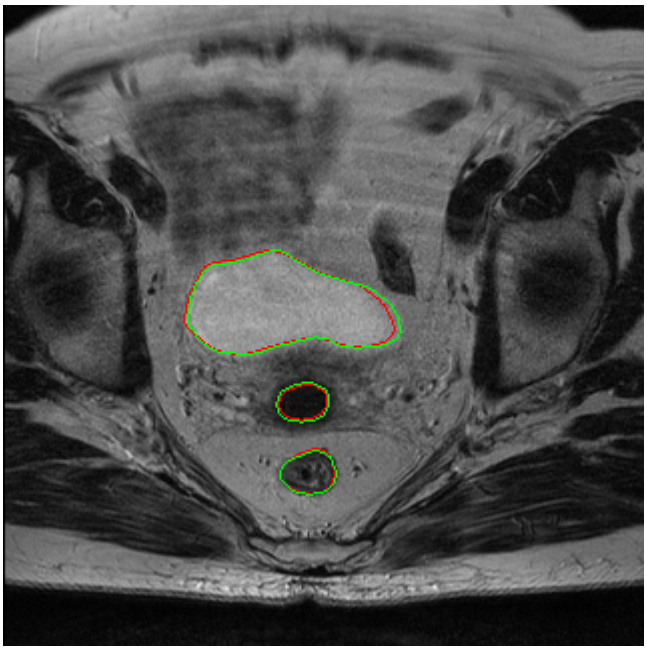

Figure 4e

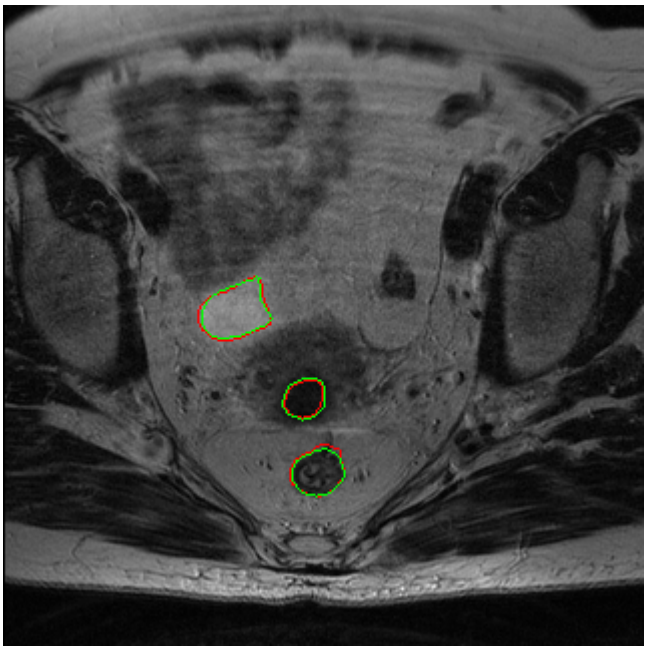

Figure 4f

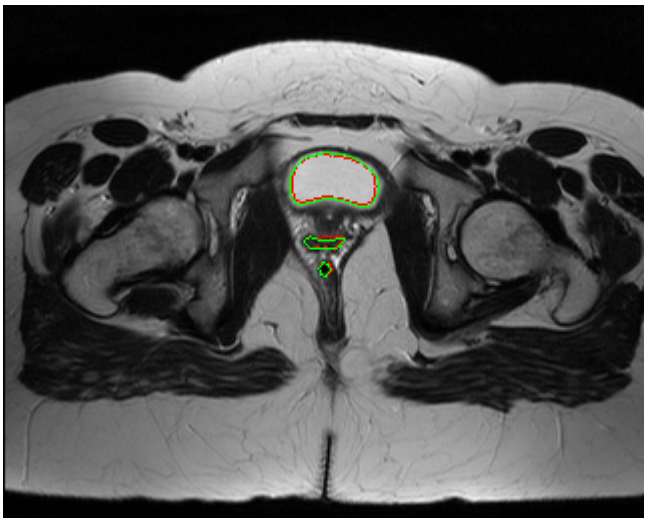

Figure 4g

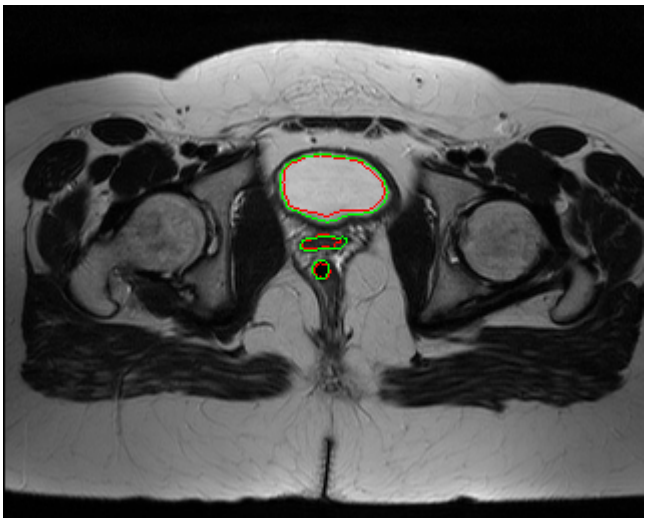

Figure 4h

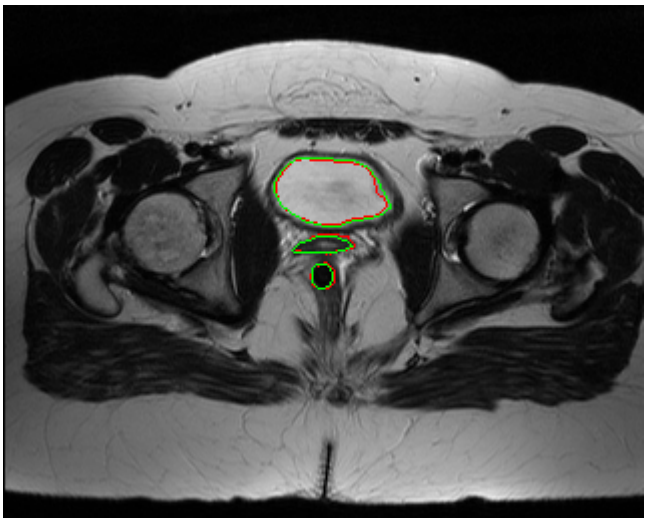

Figure 4i

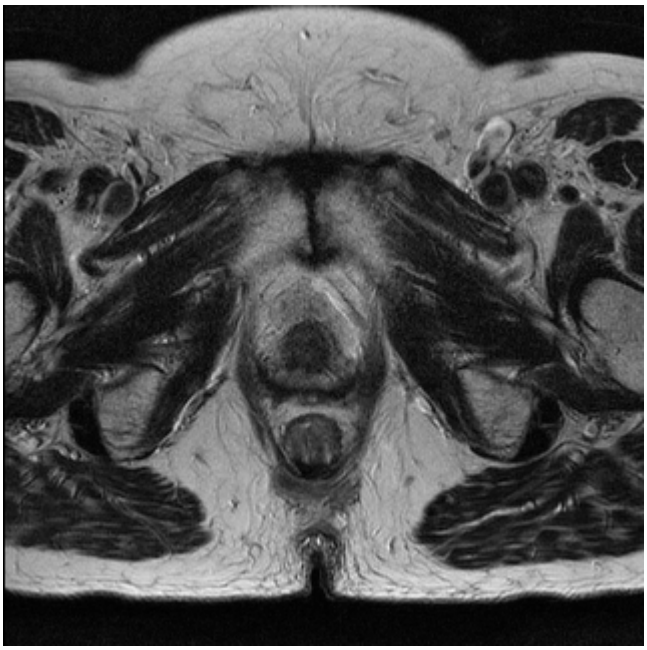

Figure 5a

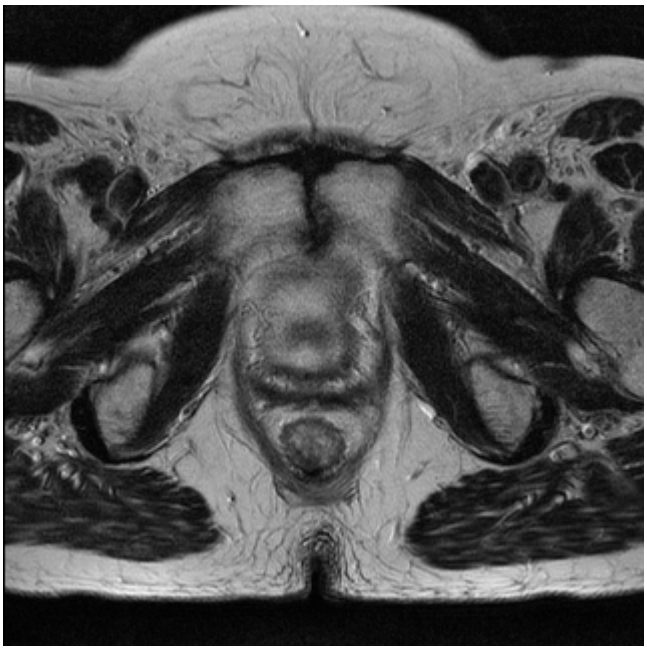

Figure 5b

Vitae

[a] **Zhen Ma** has a Master degree in Computational Science from Beihang University, and is currently pursuing his PhD degree at the University of Porto. His research interests include biomedical image processing and analysis.

[b] **Renato Natal M. Jorge** obtained his PhD degree in Mechanical Engineering from the University of Porto. Since 2007, he has been the Director of the Design and Experimental Validation Research Unit of the Institute of Mechanical Engineering. Since 2008, he has been Associate Professor of the Faculty of Engineering of the University of Porto.

[c] **Teresa Mascarenhas** is a medical doctor at São Joao Hospital, and is an expert in urogynaecology. She obtained her PhD degree in Medicine from the University of Porto. She is an Invited Associated Professor of the Faculty of Medicine of the University of Porto.

[d] **João Manuel R. S. Tavares** has a BSc degree in Mechanical Engineering, and MSc and PhD degrees in Electrical and Computer Engineering from the University of Porto. Since 2001, he has been Senior Researcher and Project Coordinator at the Institute of Mechanical Engineering and Industrial Management. Since 2011, he has been Associate Professor at the Department of Mechanical Engineering at the Faculty of Engineering of the University of Porto.